High-Power High-Speed Photodetectors—Design, Analysis, and Experimental Demonstration

L. Y. Lin, M. C. Wu, T. Itoh, *Fellow, IEEE,* T. A. Vang, R. E. Muller, D. L. Sivco, and A. Y. Cho

Abstract—A novel velocity-matched distributed photodetector (VMDP) is proposed to simultaneously achieve high saturation photocurrent and broad bandwidth. Theoretical analysis on the tradeoff between saturation power and bandwidth shows that the VMDP offers fundamental advantages over conventional photodetectors. A comprehensive theoretical model has been developed for the design and simulation of the VMDP. Experimentally, the VMDP with very high saturation (56-mA) photocurrent and instrument-limited 3-dB bandwidth (49 GHz) has been demonstrated. The theoretical analysis and experimental results show that the VMDP is very attractive for high-performance microwave photonic links and high-power optical microwave applications.

Index Terms— Coplanar transmission lines, millimeter-wave generation, MSM photodiodes, nonlinearities, photodetectors, optical pulse measurements, traveling-wave devices.

I. INTRODUCTION

MICROWAVE and millimeter-wave (or RF) photonic systems have received increasing attention recently because of their applications in analog fiber-optic links, cable-TV distributions, hybrid fiber-coax systems, wireless cable and wireless communication systems with fiber backbones, antenna remoting, and ultrawide-band optical processing of RF signals. High-power high-frequency photodetectors are key components of the RF photonic systems. Photodetectors with high saturation power can significantly reduce RF insertion loss, increase spurious-free dynamic range, and enhance signal-to-noise ratio of externally modulated links [1]–[3]. They are also important for optoelectronic generation of high-power microwaves and millimeter waves and optical heterodyned receivers. Significant progress has been achieved in high-speed photodetectors using both surface-illuminated [4]–[6] and waveguide approaches [7], [8]. However, the conventional high-speed photodetectors have very small absorption volume

$(\sim 1 \ \mu\text{m}^3)$ and, therefore, cannot achieve high saturation power.

The saturation of photocurrent under intense illumination is mainly due to the electric-field screening effect caused by the high concentration of photo-generated carriers. Enlarging the effective absorption volume of the photodetectors has been proposed as the most direct way to increase the saturation photocurrents. A large core waveguide photodetector (WGPD) with high saturation power has been demonstrated; however, this has occurred at the expense of bandwidth because longer detector length is required [9]. Velocity-matched traveling-wave photodetectors (first suggested in [10]) have been proposed to further increase the absorption volume [11]. However, the difficulty of combining a velocity-matched microwave transmission line with a high-speed photodiode in the same structure results in very low bandwidth [11].

In this paper, we propose and demonstrate a velocity-matched distributed photodetector (VMDP) to increase the optical saturation power without sacrificing its bandwidth or efficiency. In Section II, the principle and the device structure of the VMDP will be described. Section III presents the theoretical analysis on the tradeoffs between saturation power and bandwidth for different photodetector structures. Detailed theoretical modeling of the VMDP is described in Section IV. In Section V, the experimental data of the high-power high-speed VMDP with nanoscale metal–semiconductor–metal (MSM) photodiodes are reported. A very high saturation photocurrent of 56 mA (at 1-dB compression of quantum efficiency) and an instrument-limited 3-dB optical bandwidth of 49 GHz have been achieved.

II. PRINCIPLE OF VMDP's

The schematic drawing of the VMDP is shown in Fig. 1. It consists of an array of ultrafast photodiodes serially connected by a passive optical waveguide. The output photocurrents are collected by a separate velocity-matched microwave transmission line with 50-Ω impedance. Because of velocity matching, the photocurrents from each photodiode are summed up *in phase*, and the overall efficiency of the VMDP can still be high even though the efficiency of the individual photodiodes may be very low [12]–[14]. As shown in Fig. 2, the microwave velocity of typical microwave transmission lines on semiconductor substrate is about 35% faster than that of the optical waves. The microwave velocity can be slowed down by periodic capacitance loading [15], which can be achieved by the capacitance of the active photodi-
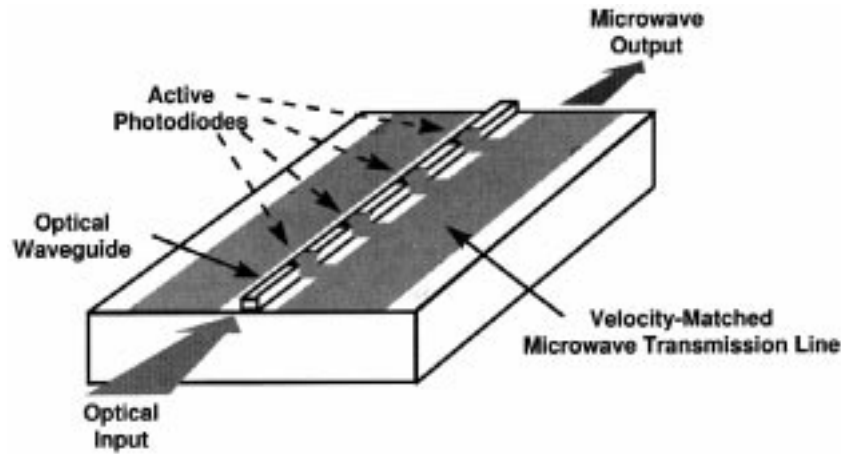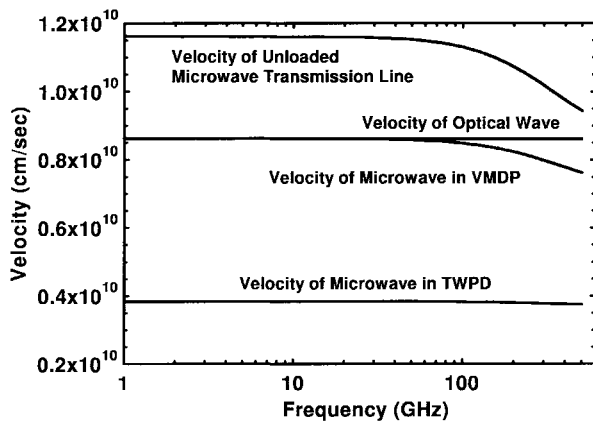
Fig. 1. The schematic drawing of the VMDP.

Fig. 2. The velocity of the optical waves as well as the microwave velocities in the VMDP, TWPD, and the unloaded microwave transmission line versus microwave frequency.

Fig. 3. Schematic structures of the (a) SIPD, (b) WGPD, (c) TWPD, and (d) VMDP.

odes themselves with properly designed size and spacing. Very good velocity matching can be achieved over a broad frequency range (1–100 GHz). For frequency higher than 100 GHz, slight velocity mismatch starts to develop due to the dispersion of the microwave transmission line. Compared with the traveling-wave photodetector (TWPD) with the microwave transmission line directly built on top of the photodiode [8], the velocity mismatch has been greatly reduced.

One unique advantage of the VMDP is that the optical waveguide, photodiodes, and microwave transmission line are separated and, therefore, can be independently optimized. The photodiodes are optimized for high-speed operation. The optical waveguide is optimized for large optical mode size (for high saturation power), low coupling loss, and single-mode operation. The microwave transmission line is optimized for impedance and velocity matching. The bandwidth of the VMDP is essentially the same as that of a single photodiode, which can be made very fast (as in conventional ultrafast photodiodes). All photodiodes are kept below saturation by coupling a small portion of optical energy into each photodiodes. This can be readily achieved by employing a small confinement factor for the absorption layer.
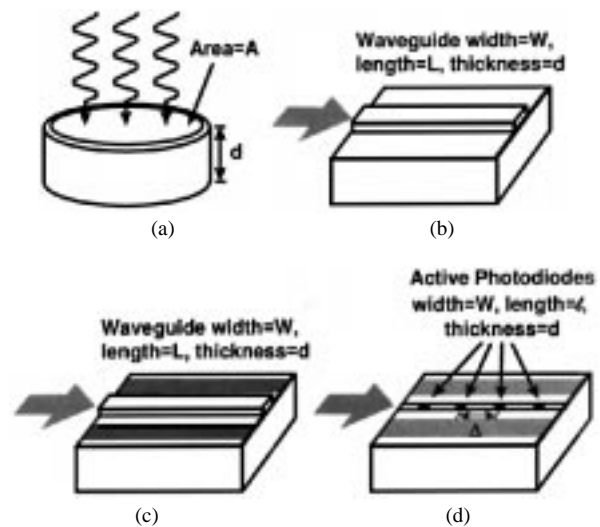
III. TRADEOFF BETWEEN SATURATION POWER AND BANDWIDTH

In this section, we present a general theory analyzing the tradeoff between saturation photocurrents and 3-dB bandwidth of four generic types of photodetectors:

1) surface-illuminated photodetector (SIPD);
2) WGPD;
3) TWPD without velocity matching [8];
4) VMDP.

In contrast to the numerical analysis of the nonlinearities in p-i-n SIPD's [16], an analytic approach with closed-form expressions are pursued here. The schematic drawings for the four photodetectors are illustrated in Fig. 3. The geometries of the photodetectors are related to the saturation photocurrent I_{SAT} through the following analysis. For waveguide-type photodetectors WGPD, TWPD, and VMDP, the quantum efficiency depends on both the detection length and the confinement factor Γ. The quantum efficiency of the WGPD is expressed as

$$\eta_{WGPD} = 1 - e^{-\alpha \Gamma L} \qquad (1)$$

where α is the absorption coefficient and L is the detector length. For a TWPD and VMDP with matched input impedance, half of the photocurrent is absorbed by the 50-Ω matching input impedance. Therefore, their quantum efficiencies are given by

$$\eta_{\text{TWPD}} = \frac{1 - e^{-\alpha\Gamma L}}{2} \qquad (2)$$

$$\eta_{\text{VMDP}} = \frac{\eta_0}{2} \frac{1 - ((1 - \eta_0)\kappa^2)^N}{1 - (1 - \eta_0)\kappa^2}. \qquad (3)$$

In (3), $\eta_0 = 1 - e^{-\alpha\Gamma\ell}$ is the quantum efficiency of the individual photodiode in the VMDP, N is the number of active photodiodes, and κ is the field coupling efficiency for the wave functions between active and passive waveguide regions. Theoretical simulation for the VMDP indicates that $\kappa \sim 98\%$ can be achieved (see Section IV-C). Assuming unity fiber-detector coupling efficiency and no trapping of the photo-generated carriers, the saturation photocurrents are expressed as

$$I_{\text{SAT, SIPD}} = q \int_0^d A P_0 \alpha e^{-\alpha x} \, dx = A I_S \qquad (4)$$

for SIPD, where d is the absorption layer thickness, A is the detector area, P_0 is the incident photon flux $(1/\mu m^2/s)$ at saturation, and I_S is the saturation photocurrent density per unit area. The I_S depends on physical structures and bias conditions, and more experimental data are necessary to determine the exact value of I_S. Here, for comparing I_{SAT} of different photodetector structures under the same bias condition, i.e., same electric field profile across the absorption region, a constant I_S of 0.025 mA/μm^2 [16] has been assumed. In general, any change or improvement of I_S should be applicable to all photodetector structures. For waveguide-type photodetectors

$$I_{\text{SAT, WGPD}} = q \int_0^L W \frac{d}{\Gamma} P_0 \alpha \Gamma e^{-\alpha\Gamma x} \, dx = \frac{W}{\alpha\Gamma} I_S \eta_{\text{WGPD}} \qquad (5)$$

$$I_{\text{SAT, TWPD}} = \frac{1}{2} q \int_0^L W \frac{d}{\Gamma} P_0 \alpha \Gamma e^{-\alpha\Gamma x} \, dx = \frac{W}{\alpha\Gamma} I_S \eta_{\text{TWPD}} \qquad (6)$$

$$\begin{aligned} I_{\text{SAT, VMDP}} &= q \int_0^\ell W \frac{d}{\Gamma} P_0 \alpha \Gamma e^{-\alpha\Gamma x} \, dx \\ &\quad + \kappa^2 e^{-\alpha\Gamma\ell} q \int_0^\ell W \frac{d}{\Gamma} P_0 \alpha \Gamma e^{-\alpha\Gamma x} \, dx \\ &\quad + \cdots + \kappa^{2\cdot(N-1)} e^{-\alpha\Gamma(N-1)\ell} \\ &\quad \times q \int_0^\ell W \frac{d}{\Gamma} P_0 \alpha \Gamma e^{-\alpha\Gamma x} \, dx \\ &= \frac{W}{\alpha\Gamma} I_S \eta_{\text{VMDP}}. \end{aligned} \qquad (7)$$

From (1) to (7), the detector area A of the SIPD, the waveguide length L of the WGPD and TWPD, and the number of active photodiodes N of the VMDP can be expressed as a function of quantum efficiency and I_{SAT}. The waveguide width W is

chosen to be 3 μm for the simulation such that single-mode propagation can be achieved for most waveguide structures.

The 3-dB optical bandwidth of the SIPD and WGPD is determined by the carrier transit time [17] and the parasitic RC time limitation

$$f_{3\,\text{dB}} = \left(2.2 \frac{d}{V} + 2\pi \frac{R_L \varepsilon A}{d} \right)^{-1} \qquad (8)$$

where V is the carrier drift velocity $(= 8 \times 10^6$ cm/s$)$, A is the detector area $(=W \times L$ for WGPD$)$, and R_L is the load resistance $(= 50 \; \Omega)$. In the TWPD and VMDP, it is further limited by the velocity mismatch between the optical wave and the generated microwave (the velocity mismatch is minimized in the VMDP) as follows:

$$f_{3\,\text{dB}} = \left(2.2 \frac{d}{V} + 2\pi \frac{\rho\varepsilon}{d} + 2\pi L \frac{V_o - V_e}{V_o V_e} \right)^{-1},$$
$$\text{for TWPD} \quad (9)$$

$$f_{3\,\text{dB}} = \left(2.2 \frac{d}{V} + 2\pi \frac{\rho\varepsilon}{d} + 2\pi (N-1)\Delta \frac{V_o - V_e}{V_o V_e} \right)^{-1},$$
$$\text{for VMDP} \quad (10)$$

where $\rho = 10^{-6} \; \Omega\cdot$cm^2 is the contact resistivity, Δ is the period between active photodiodes in the VMDP, and V_o and V_e are the velocities of optical wave and microwave, respectively. The first term represents the transit time, the second term is the RC time constant, and the third term accounts for the velocity mismatch with a matched input termination. Because of the traveling-wave property of the TWPD and VMDP, the parasitic RC bandwidth is limited by the contact resistivity instead of the load resistance as in the lumped devices SIPD and WGPD [18]. For traveling-wave type photodetectors with internal quantum-efficiency approaching unity, the effective detection length is equal to the modal absorption length [18]. However, the analysis shown in this section provides a general argument without requiring any assumption on internal quantum efficiency. Therefore, the detector length derived from its relation with quantum efficiency, (2) and (3) are used for (9) and (10).

The geometries of the photodetectors as functions of quantum efficiency and I_{SAT} are substituted into (8)–(10). For any given I_{SAT} and quantum efficiency, the 3-dB optical bandwidth is then maximized for each photodetector structure by optimizing the absorption layer thickness $\partial f_{3\,\text{dB}} / \partial d = 0$. Fig. 4 shows I_{SAT} versus $f_{3\,\text{dB}}$ thus found for the SIPD, WGPD, TWPD, and VMDP. The quantum efficiency is assumed to be 40% for WGPD, TWPD, and VMDP. The quantum efficiency of the SIPD is not an independent parameter and depends on the absorption-layer thickness. Its value varies from 83.8% at 10 GHz to 8.7% at 200 GHz. Single-pass absorption for the SIPD has been assumed for our analysis. The quantum efficiency of the SIPD can be enhanced by applying multipass resonant absorption (resonantly enhanced photodetectors); however, the spectral bandwidth of the photodetector becomes very narrow. For the VMDP, an average velocity matching of 99% $(V_o = 8.615 \times 10^9$ cm/s, $V_e = 0.99 \; V_o)$ is assumed. For the TWPD, the microwave velocity is assumed to vary from 35% [8] to 80%
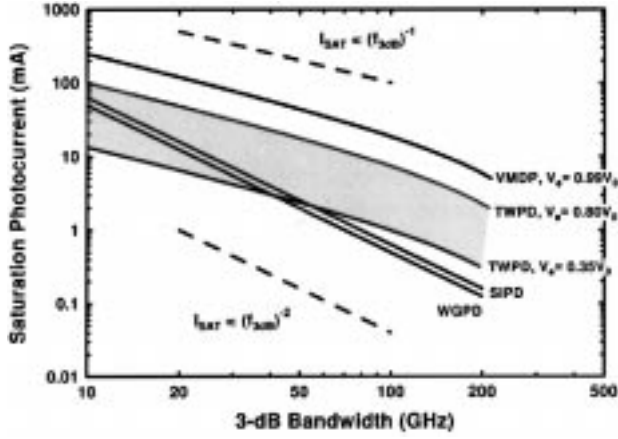
Fig. 4. The tradeoff between saturation photocurrent and 3-dB optical bandwidth for the SIPD, WGPD, velocity-mismatched TWPD, and VMDP.

Fig. 5. Contour plots for the maximum saturation photocurrent in the plane of $f_{3\,\mathrm{dB}}$ versus quantum efficiency.

TABLE I
FOM FOR HIGH-POWER, HIGH-SPEED PHOTODETECTORS

	FIGURE OF MERIT (FOM)
SIPD	$I_{SAT} \cdot (f_{3dB})^2 = \dfrac{I_S V}{17.6\pi R_L \varepsilon}$
WGPD	$I_{SAT} \cdot (f_{3dB})^2 = \dfrac{I_S V}{17.6\pi R_L \varepsilon} \cdot \dfrac{\eta}{-\ln(1-\eta)}$
TWPD	$I_{SAT} \cdot f_{3dB} = \dfrac{I_S W}{2\pi} \cdot \dfrac{V_o V_e}{V_o - V_e} \cdot \dfrac{\eta}{-\ln(1-2\eta)}$
VMDP	$I_{SAT} \cdot f_{3dB} = \dfrac{I_S W \ell}{2\pi\Delta} \cdot \dfrac{V_o V_e}{V_o - V_e} \cdot \dfrac{\eta}{-\ln(1-2\eta)}$

of the lightwave velocity to illustrate the effect of velocity-mismatching. Two interesting trends are observed in Fig. 4: $I_{\mathrm{SAT}} \propto 1/(f_{3\,\mathrm{dB}})^2$ for the two lumped photodetectors (SIPD and WGPD), while $I_{\mathrm{SAT}} \propto 1/(f_{3\,\mathrm{dB}})$ for the two traveling-wave type photodetectors (TWPD and VMDP) for $f_{3\,\mathrm{dB}} \leq$ 100 GHz. The physical interpretations are as follows. The saturation photocurrent is proportional to the effective active area, or square of the linear dimension of the detector, which is inversely proportional to the 3-dB bandwidth. Therefore, I_{SAT} is proportional to $1/(f_{3\,\mathrm{dB}})^2$. For the traveling-wave type photodetectors, the parasitic RC bandwidth is irrelevant to the dimensions of the active area. Therefore, I_{SAT} is only proportional to $1/(f_{3\,\mathrm{dB}})$.

Thus, the figure-of-merit (FOM) of high-power high-speed photodetectors can be defined from the results of simulations. The results are summarized in Table I, where $\kappa \sim 100\%$ has been assumed for the VMDP to show its fundamental limitation. The two lumped photodetectors, SIPD and WGPD, have similar performance on I_{SAT}, as shown in Fig. 4. However, WGPD can maintain high quantum efficiency when operated in a high-frequency region [17], whereas the quantum efficiency of the SIPD drops as the 3-dB bandwidth increases. This is evident from Fig. 5, which shows the contour plots of the maximum saturation photocurrent in the plane of $f_{3\,\mathrm{dB}}$ versus quantum efficiency. At sufficiently high frequencies, the saturation photocurrent of TWPD becomes higher because the traveling-wave effect eliminates the parasitic resistance loading from the matched circuit [18]; nevertheless, it is limited by the velocity mismatch. The VMDP has the highest saturation photocurrent because the velocity-matching permits long detector length. Therefore, large saturation photocurrent can be achieved without sacrificing bandwidth and efficiency.

The above analysis assumes that all detectors employ p-i-n structure for a general argument. For other detector structures, correspondent expressions for the RC bandwidth terms should be employed. For example, the exact expressions in [6] for capacitance and resistance should be used for MSM detectors. Qualitatively, as the capacitance of the MSM detectors is proportional to the detector lengths, while the resistance is inversely proportional to the detector lengths for the same
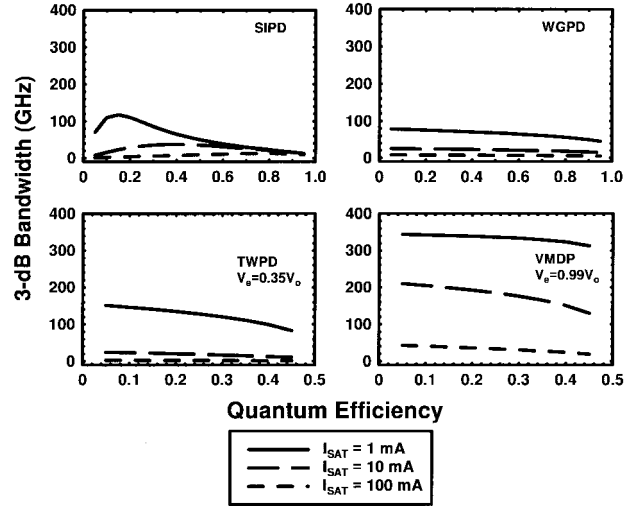
MSM finger structures, the RC bandwidth limitation remains independent of detector length for traveling-wave type photodetectors. The tradeoff between I_{SAT} and $f_{3\,\mathrm{dB}}$ is still similar to Fig. 4.

IV. THEORETICAL MODELING OF VMDP

A. Equivalent Circuit of VMDP

The VMDP is modeled as a microwave transmission line with periodically loaded photodiodes [19], as shown in Fig. 6. The equivalent circuit of the VMDP consists of an array of unit cells comprising a section of transmission line of length Δ, a shunt photodiode admittance Y, and a current source $i'_{\mathrm{ph},n}$. The current source $i'_{\mathrm{ph},n}$ is related to the photocurrent from individual photodiode $i_{\mathrm{ph},n}$ by

$$i'_{\mathrm{ph},n} = \frac{1}{1 + j(\omega/\omega_c)} i_{\mathrm{ph},n} \qquad (11)$$

through the Norton equivalent-circuit analysis. Where $\omega_c = (R_s C_p)^{-1}$ is the RC-limited frequency of the photodiode, R_s is the series resistance and C_p is the capacitance of the photodiode. The admittance of the photodiode is

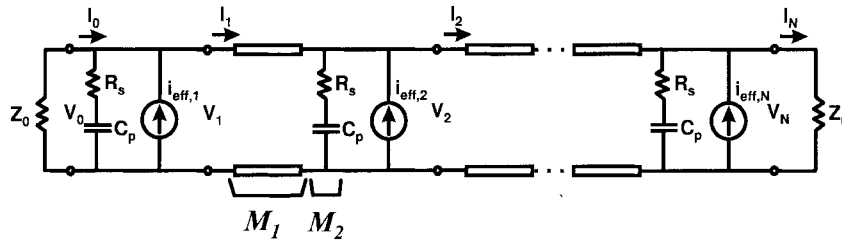$$Y = \frac{1}{R_s + 1/j\omega C_p}. \qquad (12)$$

Fig. 6.   Equivalent circuit of the VMDP.

The circuit analysis of the VMDP is formulated using the transmission matrix method [19]

$$
\begin{bmatrix} V_{n+1} \\ I_{n+1} \end{bmatrix} = \mathbf{M_2} \cdot \mathbf{M_1} \cdot \begin{bmatrix} V_n \\ I_n \end{bmatrix} + \begin{bmatrix} 0 \\ i'_{\mathrm{ph},\,n+1} \end{bmatrix}
$$
$$
\times \exp[-j\beta_{\mathrm{opt}}(f) \cdot \Delta \cdot n]
$$
$$
= \mathbf{M_2} \cdot \mathbf{M_1} \cdot \begin{bmatrix} V_n \\ I_n \end{bmatrix} + P_{\mathrm{in}} \begin{bmatrix} 0 \\ \eta_0((1-\eta_0)\kappa^2)^n \end{bmatrix}
$$
$$
\times \exp[-j\beta_{\mathrm{opt}}(f) \cdot \Delta \cdot n] \cdot \frac{1}{1 + j\omega/\omega_c} \quad (13)
$$

where $\beta_{\mathrm{opt}}(f)$ is the phase coefficient of the optical wave, P_{in} is the optical power coupled into the photodetector, and η_0 is the quantum efficiency of the individual photodiode. The transmission matrix of the transmission line segment is given by

$$
\mathbf{M_1} = \begin{bmatrix} \cosh(\gamma(f)\Delta) & \sinh(\gamma(f)\Delta)Z(f) \\ \sinh(\gamma(f)\Delta)\frac{1}{Z(f)} & \cosh(\gamma(f)\Delta) \end{bmatrix}^{-1} \quad (14)
$$
$$
\gamma(f) = \alpha(f) + j\beta(f) \quad (15)
$$

where $Z(f)$ is the characteristic impedance, and $\alpha(f)$ and $\beta(f)$ are the total loss and phase coefficient of the microwave transmission line, respectively. The transmission matrix for the photodiode is

$$
\mathbf{M_2} = \begin{bmatrix} 1 & 0 \\ -Y(f) & 1 \end{bmatrix}. \quad (16)
$$

By applying (13) recursively, V_N and I_N can be expressed as a function of V_o, I_0, and η_0. The relations between V_o, I_0, and between V_N, I_N are determined by the terminating impedance of the microwave transmission line. The homogeneous solution of V_N and I_N (denoted as V'_N and I'_N) are obtained by setting V_o and I_0 to zero and applying (13) iteratively. By superposition principle, the actual V_N and I_N can be derived from

$$
\begin{bmatrix} V_N \\ I_N \end{bmatrix} = \begin{bmatrix} V'_N \\ I'_N \end{bmatrix} + (\mathbf{M_2} \cdot \mathbf{M_1})^N \mathbf{M_1}^{-1} \begin{bmatrix} 1 \\ -\frac{1}{Z_0} \end{bmatrix} \cdot V_o. \quad (17)
$$

In (17), it is assumed that the transmission line is matched with Z_0 at the input end, as shown in Fig. 6. For the case of open-circuit input termination, the value of Z_0 in (17) should be set to ∞. The output impedance is matched ($V_N/I_N = Z_0$) in both cases.

To simulate the overall performance of the VMDP, the transit-time frequency response of the photodiodes, loss and dispersion of the microwave transmission line, and optical coupling loss should be considered. These will be discussed in the following sections. The optical propagation loss in

the passive waveguide adds an exponential decay to the photocurrent in (13). However, optical loss depends on the waveguide fabrication technique and loss as low as 0.1 dB/cm has been reported [20]. Therefore, it is not included in this paper.

B. Microwave Transmission Line

1) Dispersion and Impedance: Coplanar strips (CPS's) are employed as the microwave transmission line for the VMDP. In the current VMDP design, the CPS has a metal line width w equal to 91 μm for both the signal and ground lines. The spacing s between the metal lines is 31 μm. The thickness t of the metal lines is 0.375 μm. The semi-insulating GaAs substrate has a dielectric constant ε_r equal to 12.9 and thickness h equal to 150 μm.

The dispersion characteristics of coplanar transmission lines has been modeled numerically and analytically by [21] and experimentally verified by [22] on semi-insulating GaAs substrate. The effective dielectric constant $\varepsilon_{\mathrm{eff}}(f)$ can be expressed by the empirical formula

$$
\varepsilon_{\mathrm{eff}}(f) = \left[\sqrt{\varepsilon_{\mathrm{re}}^t} + \frac{\sqrt{\varepsilon_r} - \sqrt{\varepsilon_{\mathrm{re}}^t}}{1 + a(f/f_{\mathrm{TE}})^{-b}} \right]^2 \quad (18)
$$

where $\varepsilon_{\mathrm{re}}^t$ is the effective dielectric constant of the CPS, taking into account the transmission-line metal thickness [23]–[25], and f_{TE} is the cutoff frequency for the lowest order TE mode. It was found that $b \approx 1.8$ is independent of the dimensions of CPS, while a is related to the transmission-line geometry [21]. The phase velocity and phase coefficient of the transmission line are, therefore, expressed as

$$
v_{\mathrm{ph}}(f) = \frac{c}{\sqrt{\varepsilon_{\mathrm{eff}}(f)}} \quad (19)
$$
$$
\beta(f) = 2\pi \frac{f}{c} \sqrt{\varepsilon_{\mathrm{eff}}(f)}. \quad (20)
$$

The characteristic impedance of the CPS is related to the transmission-line geometry and the effective dielectric constant by [26]

$$
Z_0(f) = \frac{120\pi}{\sqrt{\varepsilon_{\mathrm{eff}}(f)}} \cdot \frac{K(k_e)}{K'(k_e)} \quad (21)
$$
$$
k_e = \frac{s_e}{s_e + 2w_e} \quad (22)
$$
$$
K(k_e) = \int_0^{\pi/2} \frac{d\phi}{\sqrt{1 - k_e^2 \sin^2 \phi}} \quad (23)
$$
$$
K'(k_e) = K(k'_e), \quad k'_e = \sqrt{1 - k_e^2} \quad (24)
$$

where w_e and s_e are the effective values of metal strip width and spacing due to the effect of finite-metal line thickness [23].

2) Effect of Periodic Loading: The transmission line in VMDP is periodically loaded with active photodiodes. For a low-frequency region where the spacing between the photodiodes is small compared to the wavelength, the effect of periodic loading on the phase velocity of the microwave is given by [15]

$$v_L(f) = \left(\sqrt{\left(C_M(f) + \frac{C_{p,\text{eq}}}{\Delta} \right) L_M(f)} \right)^{-1} \quad (25)$$

where $C_M(f)$ is the equivalent capacitance and $L_M(f)$ is the equivalent inductance per unit length of the transmission line and $C_{p,\text{eq}}$ is the effective capacitance of the photodiode. The $C_M(f)$ can be expressed as [23]

$$C_M(f) = \varepsilon_{\text{eff}}(f)\varepsilon_0 \frac{K'(k_e)}{K(k_e)}. \quad (26)$$

The $C_{p,\text{eq}}$ is related to both R_s and C_p by

$$\frac{1}{C_{p,\text{eq}}} = \frac{1}{C_p} + j\omega R_s. \quad (27)$$

Nevertheless, the effect of the photodiode resistance is small compared to the capacitance loading.

The impedance of the periodically loaded transmission line can be derived under the same assumption [15]

$$Z_L(f) = \sqrt{\frac{L_M(f)}{C_M(f) + \frac{C_{p,\text{eq}}}{\Delta}}}. \quad (28)$$

In the current VMDP design, the MSM photodiode is chosen as the active photodiode because of its low parasitics and ease of integration with the coplanar microwave transmission line. The parasitic capacitance and resistance of the MSM photodiode can be calculated using the equations in [6]. The current MSM finger pattern has the following geometry: metal line width $= 0.3$ μm, finger pitch $= 0.5$ μm, metal thickness $= 500$ Å, finger length $= 18$ μm, overlap finger length between electrodes $= 7$ μm, and the period between active photodiodes $= 10\times$ (length of the MSM photodiode). Using these parameters, the phase velocity and the impedance of the periodically-loaded transmission line in VMDP versus frequency are plotted in Fig. 7. Also shown in Fig. 7 is the velocity of the optical wave in the VMDP obtained from the effective refractive index of the optical waveguide, which will be discussed in Section IV-C. The designed VMDP has matched velocities and impedance.

3) Loss Coefficients: The microwave losses in CPS's include conductor loss, dielectric loss, and radiation loss. For conductor loss [23]

$$\alpha_c(f) = 17.34 \frac{Z_s(f)}{Z_L(f)} \frac{P'}{\pi s_e} \left(1 + \frac{w_e}{s_e} \right)$$
$$\times \left\{ \frac{\frac{1.25}{\pi} \ln \frac{4\pi w_e}{t} + 1 + \frac{1.25t}{\pi w_e}}{\left[1 + 2\frac{w_e}{s_e} + \frac{1.25t}{\pi s_e} \left(1 + \ln \frac{4\pi w_e}{t} \right) \right]^2} \right\}$$
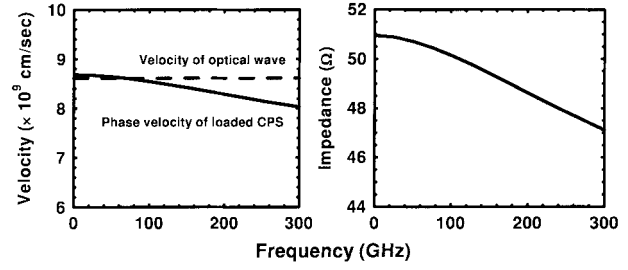$$\text{(dB/unit length)} \quad (29)$$

Fig. 7. Phase velocity and impedance of the periodically loaded CPS in the VMDP and the velocity of the optical wave versus microwave frequency.
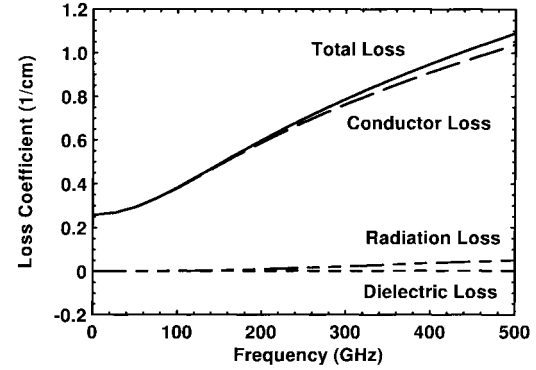

Fig. 8. Conductor, dielectric, radiation, and total loss coefficients for the CPS in the VMDP.

where $Z_s(f)$ is the surface impedance of the conductor [27]. The P' is given by

$$P' = \left(\frac{K(k_e)}{K'(k_e)} \right)^2 \frac{k_e}{(1 - k'_e)\sqrt{(k'_e)^3}}. \quad (30)$$

For dielectric loss [23]

$$\alpha_d(f) = 27.3 \frac{\varepsilon_r}{\sqrt{\varepsilon_{\text{eff}}(f)}} \frac{\varepsilon_{\text{eff}}(f) - 1}{\varepsilon_r - 1} \frac{\tan(\delta(f))}{c/f}$$
$$\text{(dB/unit length)} \quad (31)$$

where $\delta(f)$ is the skin depth of the conductor. The radiation loss can be expressed as [22]

$$\alpha_r(f) = \pi^5 \frac{3 - 2\sqrt{2}}{2} \sqrt{\frac{\varepsilon_{\text{eff}}(f)}{\varepsilon_r}} \left(1 - \frac{\varepsilon_{\text{eff}}(f)}{\varepsilon_r} \right)^2$$
$$\times \frac{(s_e + 2w_e)^2}{c^3 K(k_e)K'(k_e)} f^3 \text{ (dB/unit length).} \quad (32)$$

Fig. 8 shows the conductor, dielectric, radiation, and total loss coefficients versus frequency for the CPS in the VMDP. For this CPS geometry, the dominant loss mechanism is the conductor loss.

C. Optical Waveguide

The epitaxial layer structure of the device consists of a 3-μm-thick Al$_{0.25}$Ga$_{0.75}$As lower cladding layer, a 0.5-μm-thick Al$_{0.15}$Ga$_{0.85}$As waveguide core layer, a 0.2-μm-thick Al$_{0.35}$Ga$_{0.65}$As upper cladding layer, and a 0.2-μm-thick low-temperature (LT) grown (200 °C) GaAs absorbing layer. The absorbing layer is designed to be on the top

surface and evanescently coupled to the passive waveguide to facilitate device contact and fabrication. A 3-μm-wide optical ridge waveguide is formed by wet chemical etching of the $Al_{0.35}Ga_{0.65}As$ cladding layer by 0.1-μm depth. To achieve high saturation power, the confinement factor of the MSM absorbing layer is designed to be very low (equal to 1.53%). Furthermore, the structure is designed to have a large-core waveguide which results in a more symmetric circular far-field pattern to better match that of the optical fiber. Therefore, higher coupling efficiency can be obtained.

The one-dimensional (1-D) effective indexes of refraction of the planar waveguide in the lateral region (N_I) and the guided region (N_{II}) are solved first using the multilayer stack theory [28]. For optical wavelength at 860 nm, only the fundamental mode exists in the waveguide. The obtained effective indexes are $N_I = 3.4809$ for the lateral region, $N_{II} = 3.4832$ and $3.4850 + 0.001\,08i$ for the guided region in the passive optical waveguide and the active photodiode sections, respectively. The imaginary part of effective refractive index in the photodiode region is due to optical absorption in the GaAs absorbing layer. The effective refractive index N_{eff} of the ridge waveguide in the VMDP can thus be obtained using the effective-index method [29]. The N_{eff} for the optical waveguide is found to be 3.4823. The velocity of the optical wave can, therefore, be determined from the following equation:

$$v_{opt} = \frac{c}{N_{eff}} = 8.615 \times 10^9 \text{ (cm/s)}. \tag{33}$$

The optical wave function in the waveguide can be calculated using the same transfer matrix approach [28] after solving the effective refractive index N_{II} in the guided region. The real part of the simulated wave functions in the passive waveguide and the active photodiode regions are shown in Fig. 9. The optical wave is mainly confined in the passive core region and coupled evanescently to the top GaAs absorbing region in the active section. The confinement factor Γ is defined by the percentage of the optical-field intensity confined in the GaAs layer

$$\Gamma = \frac{\int_{x_a}^{x_b} \left| E_y^{active}(x) \right|^2 dx}{\int_{-\infty}^{\infty} \left| E_y^{active}(x) \right|^2 dx} \tag{34}$$

where x_a is the coordinate of $Al_{0.35}Ga_{0.65}As$/GaAs interface, and x_b is the coordinate of GaAs/Air interface. Because of the low confinement factor of the VMDP, the optical transition between the passive waveguide and active photodiode sections are relatively smooth. The field coupling efficiency between the passive waveguide and the photodiode region can be calculated by the overlap integral of the wave functions

$$\kappa = \frac{\left| \int E_y^{active}(x) \cdot \left(E_y^{passive}(x) \right)^* dx \right|^2}{\int \left| E_y^{active}(x) \right|^2 dx \cdot \int \left| E_y^{passive}(x) \right|^2 dx}. \tag{35}$$

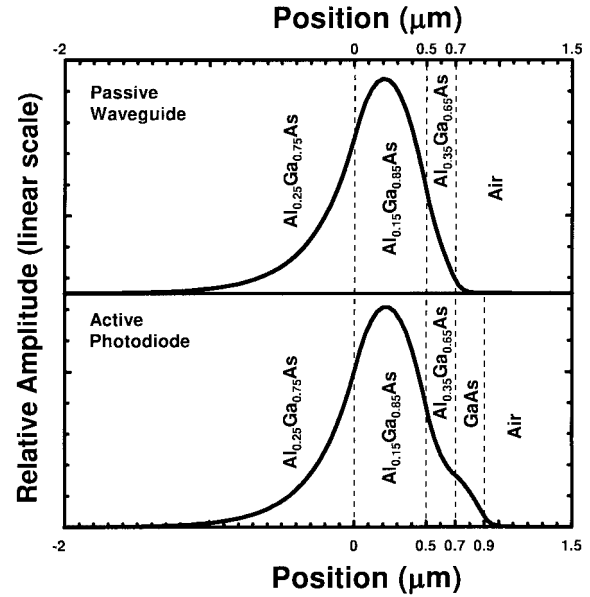The theoretical coupling efficiency κ for the designed VMDP is found to be 97.8%.

Fig. 9. The optical wave functions in the passive waveguide and the active photodiode regions of VMDP.

D. Simulated Performance of VMDP

The frequency response of the overall efficiency of the VMDP is a product of three contributing factors:

1) frequency response due to carrier transit time $(\eta_{TR}(f))$;
2) frequency response due to RC limitation of individual photodiodes $(\eta_{RC}(f))$;
3) response of the VMDP structure itself $\eta_{VMDP}(f)$.

The last includes the effects of residue velocity mismatch, microwave loss of the transmission line, and the optical coupling loss between passive and active waveguides. The overall efficiency can be expressed as

$$\eta_{ALL}(f) = \eta_{TR}(f) \cdot \eta_{RC}(f) \cdot \eta_{VMDP}(f). \tag{36}$$

The combined response of the RC limit of individual photodiodes and the VMDP structure has been derived earlier in Section IV-A. The frequency response due to transit time will be discussed in this section.

The transit time limitation arises from the finite drift velocities of carriers in the light absorption region. When the reciprocal of the optical modulation frequency becomes comparable to the time required for the generated electron–hole pairs to travel to the electrodes, the photodiode cannot fully respond to the modulation. The theoretical model developed in [30] is employed for simulating the transit-time frequency response of the MSM photodiode in the VMDP. The simulation result shows a 3-dB bandwidth of 250 GHz, assuming the saturation velocities for electrons and holes are 0.8×10^7 cm/s and 0.6×10^7 cm/s, respectively.

The high-field region of the MSM photodiode is concentrated on the surface of the diode. Therefore, there is low-field region toward the bottom of the absorption layer where the photo-generated carriers, which normally have lifetimes on the order of a few tens of picoseconds in bulk GaAs, cannot travel at saturation velocities. This results in long tails seen in
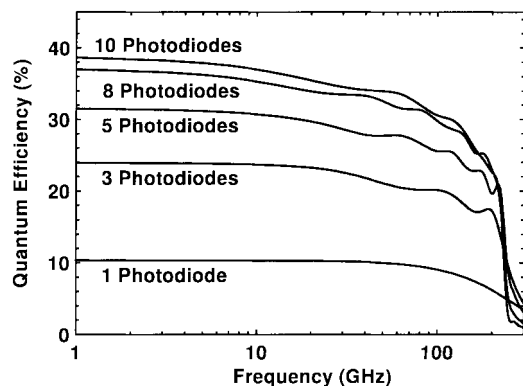
Fig. 10. Frequency responses of the VMDP with various number of active photodiodes.
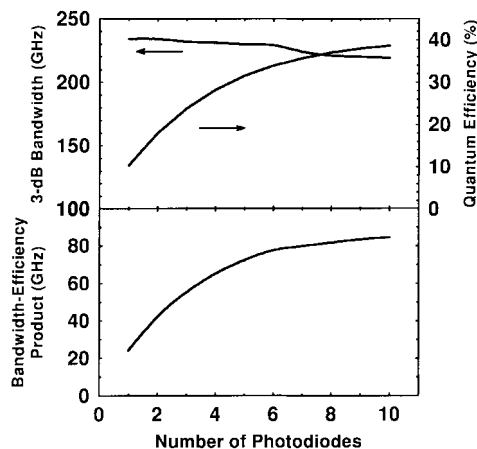

Fig. 11. 3-dB optical bandwidth, maximum quantum efficiency, and bandwidth-efficiency product of the VMDP versus the number of active photodiodes.
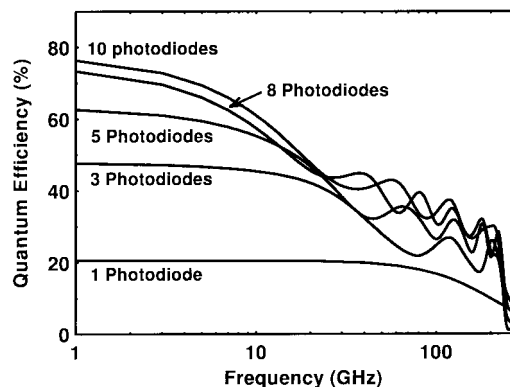

Fig. 12. Frequency responses of the VMDP with open-circuit input termination.

the time-domain response of conventional MSM photodiodes. The long tails can be suppressed by: 1) minimizing the low-field region of the photodiode and 2) introducing trapping centers in the absorption region. In the VMDP, the thickness of the absorption layer is very thin (0.2 μm, comparable to the finger spacing), and a heterostructure barrier is employed at the bottom of the absorption region to prevent carriers from spreading over to the low-field region. The finger width is also minimized to reduce the low-field region underneath the MSM fingers. In addition, the absorption layer of the MSM photodiodes is designed to be LT-GaAs, which features short carrier lifetime because of the precipitating of excess arsenic during the annealing at 600 °C to form densely packed recombination centers [31]. This results in the elimination of the long tail in the time-domain response—however, at the expense of reduced sensitivity.

The overall frequency response of the VMDP can now be simulated and the results are shown in Fig. 10. The length of each MSM photodiode is 15 μm, and the period between active photodiodes is 150 μm. The bandwidth of the VMDP with one MSM photodiode is basically the same as that of the conventional high-speed MSM photodetector [6], and can be as high as several hundred gigahertz, though the quantum efficiency is low because of the high-power design. The quantum efficiency increases with increasing number of photodiodes, with very slight decrease in the bandwidth, as shown in Fig. 11. The theoretical limit of the quantum efficiency for the VMDP (or more generally, for any TWPD's) with 50-Ω input termination is 50% since half of the photocurrent propagates in the backward direction and is absorbed by the input termination. The maximum quantum efficiency obtained here is 40%, which is limited by the nonideal optical transition between the active and passive waveguide regions (theoretical coupling efficiency is equal to 98%). A bandwidth-efficiency product over 80 GHz can be achieved if the number of photodiodes is greater than eight. The quantum efficiency of the VMDP at low frequency can be doubled by employing open-circuit input termination. However, the detector bandwidth will decrease since the microwaves reflected from the input end are not in phase with the forward traveling wave. The simulation results of the VMDP with open-circuit termination are shown in Fig. 12.

In addition to the intrinsic effect of the device, other extrinsic parameters such as optical input coupling also directly affect the measured overall efficiency. One of the main disadvantage of waveguide-type photodetectors is the low optical coupling efficiency. The VMDP is designed to have a more circular optical mode with small optical confinement; therefore, the optical coupling efficiency is higher than those of conventional WGPD's. Here, we examine the optical coupling efficiency from a low-cost spherical lensed-fiber to the VMDP. The lensed-fiber used in our experiments is made by Ericsson's Fusion Splicer FSU 925 and has a diameter of 18 μm. The theory for the lensed-fiber coupling efficiency can be found in [32]. The simulation result is shown in Fig. 13. A maximum coupling efficiency of 48% can be achieved at 13.5-μm separation between the fiber tip and the optical waveguide facet. The current coupling efficiency is limited by the nonperfect circular shape of the optical mode field for the waveguide (see Fig. 9 for the simulated wave function and [19]).

V. EXPERIMENTAL RESULTS

The schematic structure of the VMDP has been shown in Fig. 1. The scanning electron micrograph (SEM) of the VMDP is shown in Fig. 14. Nanoscale MSM photodiodes are chosen
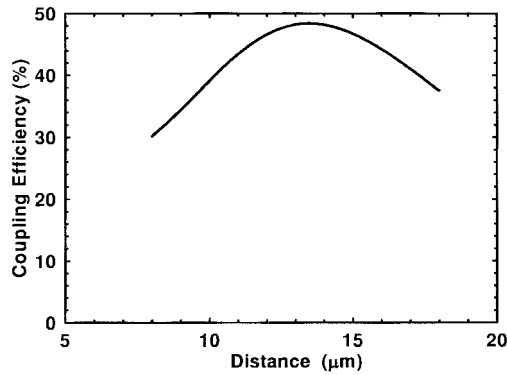
Fig. 13. The fiber coupling efficiency as a function of the distance between the lensed and fiber tip and the optical waveguide facet.

Fig. 15. S_{22} measurement of the transmission line in the VMDP using an HP 8510C network analyzer. The transmission has an impedance close to 50 Ω.

to 50 Ω (within 6% deviation) throughout the measurement range. Another important parameter to verify is the phase velocity of the periodically loaded microwave transmission line. This is measured from 0.045 to 50 GHz using an HP 8510C network analyzer. As in the impedance measurement, full two-port calibration was performed for the probes and microwave connections. Instead of the reflection coefficient, the time delay of the microwave signal between the two calibration planes (two probe tips) is measured. From the length of the transmission line between the two calibration planes, the microwave phase velocity can be determined. The result is shown in Fig. 16. The theoretically simulated phase velocity (Fig. 7) is superimposed on the experimental curve. Reasonably good agreement is obtained.

The dc quantum efficiency of the VMDP is measured using a tunable Ti:Sapphire laser as the light source. The wavelength of the laser is tuned to 860 nm. The dc photocurrent increases linearly with the input optical power varying from 0 to 60 mW. The measured external quantum efficiency is equal to 12.3% (electron/photon) for uncoated facet, which is 26% of the theoretical value (48% for the VMDP with 3 photodiodes and open-circuit input termination, see Fig. 10). The quantum efficiency of the device can be improved by optimizing the coupling efficiency of the lensed fiber (currently $\sim$ 48%) or applying antireflection (AR) coating to the VMDP facet (30% Fresnel loss), as well as improving the coupling efficiency between the passive and active waveguide regions (currently causes $\sim$ 22% more coupling loss compared to the theoretical prediction, see Fig. 20) by better controlling the etching steps in the fabrication. The propagation loss in the optical waveguide is negligible compared to these three factors.

The experimental setup for measuring the frequency response and saturation photocurrent is shown in Fig. 17. The impulse response of the VMDP is characterized first. The Ti:Sapphire laser is mode locked at 860 nm with a pulsewidth of 120 fs and a repetition rate of 80 MHz. The light is coupled into a single-mode fiber and then passes through a 3-dB fiber coupler. One branch of the 3-dB coupler is connected
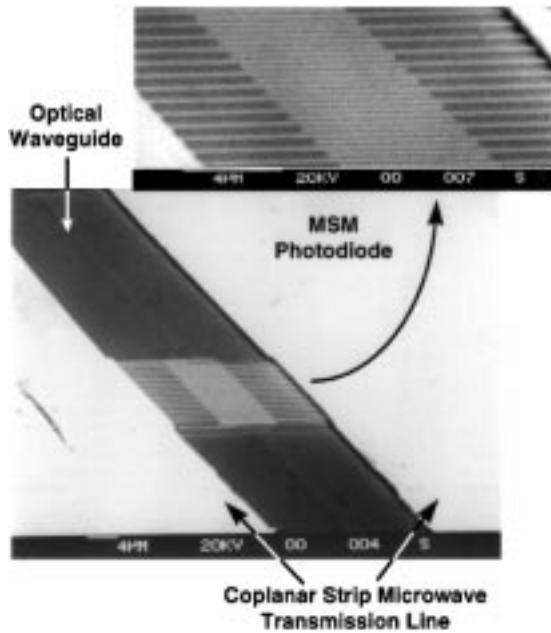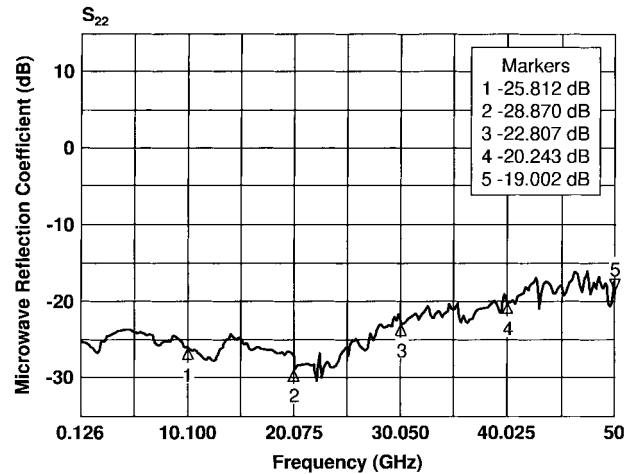

Fig. 14. The SEM micrograph of the VMDP. The inset shows the MSM photodiode.

as the active photodiodes for the current VMDP. However, the VMDP concept can be applied to other photodiode structures such as a p-i-n. The fabrication process of the MSM VMDP have been reported in [14]. In this section, we report on the experimental characterization of the VMDP, including both dc and RF measurements. The device-under-test has three active photodiodes. Each photodiode is 15-μm long, and the period between them is 150 μm. The input end of the device is not impedance-matched for higher saturation photocurrent.

First, we will discuss the characteristics of the microwave transmission line in VMDP. The impedance of the periodically loaded transmission line in VMDP is characterized from 0.126 to 50 GHz using an HP 8510C network analyzer. Two-port measurement for transmission lines was employed. Fig. 15 shows the S_{22} measurement (reflection coefficient at port 2) of the transmission line. The probe and microwave connections on port 1 has been calibrated to 50 Ω for the measurement. The impedance of the transmission line obtained from the Smith chart of the same measurement is very close
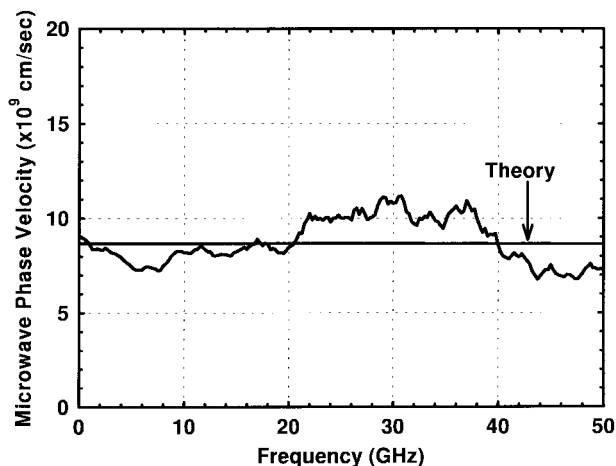
Fig. 16. The experimental and theoretical phase velocity of the periodically loaded transmission line on the VMDP. The experimental phase velocity is determined from the time-delay measurement using an HP 8510C network analyzer.
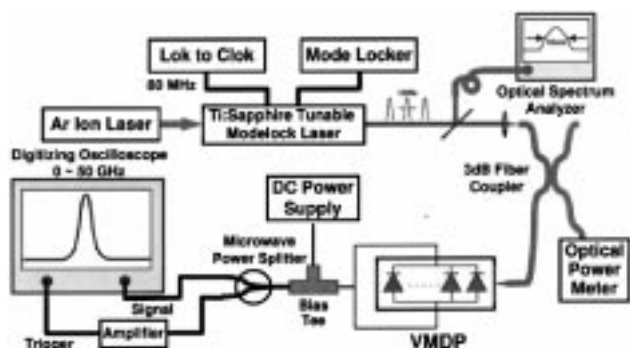

Fig. 17. The experimental setup for measuring RF response and saturation photocurrent.
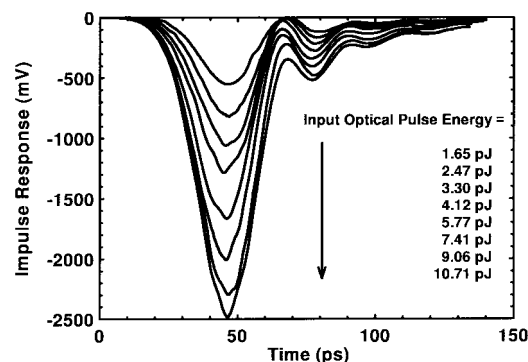

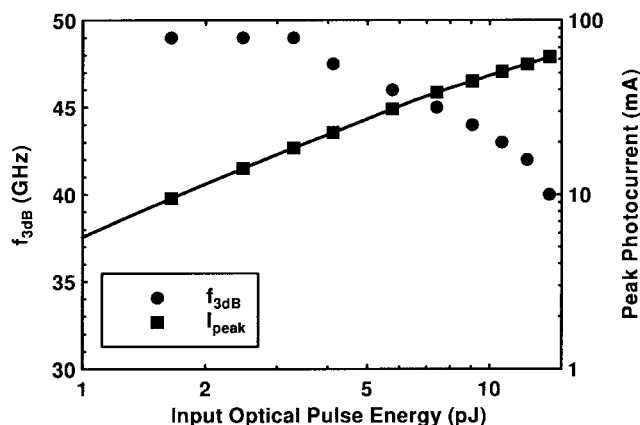Fig. 18. Impulse response of the VMDP under various illumination intensities.

Fig. 19. The 3-dB optical bandwidth and the peak photocurrent versus the input optical pulse energy for VMDP.

to an optical power meter for power monitoring. The other branch is coupled into the device using the lensed fiber. The device-under-test is biased at 4 V through a bias-tee. The generated microwave signal is collected at the output end of the transmission line by a 50-GHz high-frequency probe (Picoprobe from GGB Industries). The signal is then sent to an HP digitizing oscilloscope with 50-GHz bandwidth through a microwave cable. Part of the signal is split by a microwave power splitter and amplified to trigger the digitizing oscilloscope. The timing jitters of the measured signal are greatly reduced in this configuration.

The electrical frequency response is obtained from the Fourier transform of the impulse response, and the results have been reported in [14]. A 3-dB optical bandwidth of 49 GHz is achieved, which appears to be limited by the bandwidth of the digitizing oscilloscope.

To investigate the ac saturation effect, the impulse response of the VMDP is measured with increasing optical powers. The result is shown in Fig. 18. At low intensities, the ac quantum efficiency is equal to the dc quantum efficiency. Under intense illumination, the pulsewidth increases slightly and a long tail in the trailing edge starts to develop in the impulse response. This results in a reduction of the quantum efficiency as well as bandwidth of the photodetector. The degradation is attributed

to the electric field screening effect due to the large number of photo-generated carriers. The saturation point is defined to be at 1-dB compression of the ac quantum efficiency. The ac quantum efficiency at low-intensity illumination is obtained by dividing the number of photo-generated carriers calculated using the impulse response with the number of incident photons. Under intense illumination, the peak value of the impulse response does not increase linearly with the optical pulse energy, and the ac quantum efficiency is obtained by comparing the peak impulse response with the low-intensity illumination response. The peak photocurrent obtained by dividing the peak voltage of the impulse response with the 50-Ω load at 1-dB compression is equal to 56 mA [14]. The 3-dB optical bandwidths of the VMDP under various illumination intensities are also characterized. The experimental results are shown in Fig. 19. The bandwidth remains unchanged as the peak photocurrent increases to 19 mA ($\eta_{AC}/\eta_{DC} \sim 1$), and gradually reduces to 42 GHz when η_{AC}/η_{DC} reaches 1-dB compression.

The VMDP is expected to have similar saturation photocurrent under CW operation if proper heat sinking and facet passivation are provided. From a heat-sinking point of view, the heat generated in the VMDP is distributed along the waveguide, which is more advantageous compared to the heat-point source of lumped photodetectors. This problem is currently under investigation.
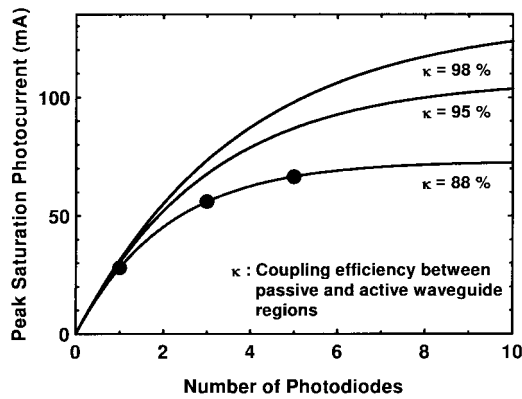
Fig. 20.   The theoretical and experimental peak-saturation photocurrents of the VMDP versus the number of photodiodes for three coupling efficiencies between passive waveguide and active photodiode regions: $k = 88\%$, 95%, and 98%.

The saturation photocurrent is also measured for the VMDP with one and five photodiodes. The results are shown in Fig. 20. The bandwidth of the VMDP with three photodiodes is the same as that of the VMDP with one photodiode, and degrades slightly when the number of the photodiodes increases to five. Also shown in Fig. 20 are the calculated saturation-peak photocurrent versus the number of photodiodes for different coupling efficiencies between the passive and active waveguide regions. Coupling efficiency affects the quantum efficiency and, therefore, the saturation photocurrent (7). Physically, lower coupling efficiency reduces the saturation photocurrent because the photodetector starts to saturate at the first photodiode, and loss of light due to nonideal coupling will reduce the photocurrents of subsequent photodiodes when the first photodiode saturates. The measured data agrees well with the curve of $\kappa = 88\%$. This coupling efficiency is somewhat lower than the theoretical value of 98%. The discrepancy is attributed to the slight over-etch during removal of the absorbing layer in the passive waveguide. By employing selective etching, better coupling efficiency is expected. The saturation peak photocurrent can be further increased to >100 mA by improving the coupling efficiency from 88% to 95% and increasing the number of photodiodes to ten.

VI. CONCLUSION

We have proposed a novel VMDP to achieve high saturation photocurrent and large bandwidth. The theoretical analysis on the tradeoff between saturation power and bandwidth shows that the VMDP offers fundamental advantages over other conventional photodetectors. Theoretical models have been developed to design and simulate the performance of the VMDP. The VMDP's with nanoscale MSM photodiodes have also been experimentally demonstrated. A very high saturation photocurrent of 56 mA and an instrument-limited 3-dB optical bandwidth of 49 GHz have been achieved. Further improvement in optical saturation power and quantum efficiency is expected with more precise control of the fabrication processes and proper AR coating for the facet. The theoretical analysis and the experimental results of the VMDP show that it can greatly improve the RF insertion loss, dynamic

range, and noise performance of analog fiber-optic links. It is also attractive for high-power optical-microwave applications and optoelectronic generation of high-power microwaves and millimeter waves.

REFERENCES

[1] C. H. Cox, "Analog fiber-optic links with intrinsic gain," *Microwave J.*, vol. 35, no. 9, pp. 92–99, 1992.
[2] ———, "Gain and noise figure in analogue fiber-optic links," *Proc. Inst. Elect. Eng.*, vol. 139, pt. J., no. 4, pp. 238–242, 1992.
[3] R. F. Kalman, J. C. Fan, and L. G. Kazovsky, "Dynamic range of coherent analog fiber-optic links," *J. Lightwave Technol.*, vol. 12, pp. 1263–1277, July 1994.
[4] Y. G. Wey, K. Giboney, J. Bowers, M. Rodwell, P. Silvestre, P. Thiagarajan, and G. Robinson, "110-GHz GaInAs/InP double heterostructure p-i-n photodetectors," *J. Lightwave Technol.*, vol. 13, pp. 1490–1499, July 1995.
[5] K. D. Li, A. S. Hou, E. Ozbay, B. A. Auld, and D. M. Bloom, "2-picosecond, GaAs photodiode optoelectronic circuit for optical correlations," *Appl. Phys. Lett.*, vol. 61, no. 26, pp. 3104–3106, 1992.
[6] S. Y. Chou and M. Y. Liu, "Nanoscale tera-hertz metal–semiconductor–metal photodetectors," *IEEE J. Quantum Electron.*, vol. 28, pp. 2358–2368, Oct. 1992.
[7] K. Kato, A. Kozen, Y. Muramoto, Y. Itaya, T. Nagatsuma, and M. Yaita, "110-GHz, 50%-efficiency mushroom-mesa waveguide p-i-n photodiode for a 1.55-μm wavelength," *IEEE Photon. Technol. Lett.*, vol. 6, pp. 719–721, June 1994.
[8] K. S. Giboney, R. L. Nagarajan, T. E. Reynolds, S. T. Allen, R. P. Mirin, M. J. W. Rodwell, and J. E. Bowers, "Travelling-wave photodetectors with 172-GHz bandwidth and 76-GHz bandwidth-efficiency product," *IEEE Photon. Technol. Lett.*, vol. 7, pp. 412–414, Apr. 1995.
[9] A. R. Williams, A. L. Kellner, and P. K. L. Yu, "Dynamic range performance of a high speed, high saturation InGaAs/InP pin waveguide photodetector," *Electron. Lett.*, vol. 31, no. 7, pp. 548–549, 1995.
[10] H. F. Taylor, O. Eknoyan, C. S. Park, K. N. Choi, and K. Chang, "Traveling wave photodetectors," *SPIE: Opt. Signal Processing Phased-Array Antennas II*, vol. 1217, pp. 59–63, 1990.
[11] V. M. Hietala, G. A. Vawter, T. M. Brennan, and B. E. Hammons, "Traveling-wave photodetectors for high-power, large-bandwidth applications," *IEEE Trans. Microwave Theory Tech.*, vol. 43, pp. 2291–2298, Sept. 1995.
[12] M. C. Wu and T. Itoh, "Ultrafast photonic-to-microwave transformer (PMT)," presented at the *IEEE LEOS Summer Topical Meeting Opt. Microwave Interactions*, Santa Barbara, CA, July 19–21, 1993.
[13] L. Y. Lin and M. C. Wu, "Ultrafast high power photodetectors," presented at the *IEEE LEOS Summer Topical Meetings*, Keystone, CO, Aug. 7–11, 1995.
[14] L. Y. Lin, M. C. Wu, T. Itoh, T. A. Vang, R. E. Muller, D. L. Sivco, and A. Y. Cho, "Velocity-matched distributed photodetectors with high-saturation power and large bandwidth," *IEEE Photon. Technol. Lett.*, vol. 8, pp. 1376–1378, Oct. 1996.
[15] R. E. Collin, *Foundations for Microwave Engineering*, 2nd ed.   New York: McGraw-Hill, 1992, ch. 8.
[16] K. J. Williams, R. D. Esman, and M. Dagenais, "Nonlinearities in p-i-n microwave photodetectors," *J. Lightwave Technol.*, vol. 14, pp. 84–96, Jan. 1996.
[17] J. E. Bowers and C. A. Burrus, "Ultrawide-band long-wavelength p-i-n photodetectors," *J. Lightwave Technol.*, vol. LT-5, pp. 1339–1350, Oct. 1987.
[18] K. S. Giboney, M. J. W. Rodwell, and J. E. Bowers, "Traveling-wave photodetectors," *IEEE Photon. Technol. Lett.*, vol. 4, pp. 1363–1365, Dec. 1992.
[19] L. Y. Lin, "High-Power, High-speed photodetectors and micromachined free-space integrated optics," Ph.D. dissertation, Elect. Eng. Dept., UCLA, Los Angeles, CA, 1996.
[20] R. J. Deri and E. Kapon, "Low-loss III–V semiconductor optical waveguides," *IEEE J. Quantum Electron.*, vol. 27, pp. 626–640, Mar. 1991.

[21] G. Hasnain, A. Dienes, and J. R. Whinnery, "Dispersion of picosecond pulses in coplanar transmission lines," *IEEE Trans. Microwave Theory Tech.*, vol. 34, pp. 738–741, June 1989.

[22] M. Y. Frankel, S. Gupta, J. A. Valdmanis, and G. A. Mourou, "Terahertz attenuation and dispersion characteristics of coplanar transmission lines," *IEEE Trans. Microwave Theory Tech.*, vol. 39, pp. 910–916, June 1991.

[23] K. C. Gupta, R. Garg, and I. J. Bahl, *Microstrip Lines and Slotlines*. Norwood, MA: Artech House, 1979, ch. 7.

[24] I. J. Bahl, "Design considerations for coplanar waveguides and coplanar strips," I.I.T., Elect. Eng. Dept., Kanpur, India, Tech. Rep., vol. 78-MW1, 1978.

[25] T. Kitazawa, Y. Hayashi, and M. Suzuki, "A coplanar waveguide with a thick metal-coating," *IEEE Trans. Microwave Theory Tech.*, vol. MTT-24, pp. 604–608, Sept. 1976.

[26] C. P. Wen, "Coplanar waveguide: A surface strip transmission line suitable for nonreciprocal gyromagnetic device application," *IEEE Trans. Microwave Theory Tech.*, vol. MTT-17, pp. 1087–1090, Jan. 1969.

[27] D. B. Rutledge, D. P. Neiktrik, and D. P. Kasilingham, *Infrared and Millimeter Waves*, K. J. Button, Ed.   New York: Academic, 1983, vol. 10, pt. 2.

[28] M. Born and E. Wolf, *Principles of Optics*.   New York: Pergamon, 1959.

[29] H. Kogelink, "Theory of optical waveguides," in *Guided-Wave Optoelectronics*, T. Tamir, Ed.   Berlin, Germany: Springer-Verlag, 1988.

[30] G. Lucovsky, R. F. Schwarz, and R. B. Emmons, "Transit-time considerations in p-i-n diodes," *J. Appl. Phys.*, vol. 35, no. 3, pp. 622–628, 1964.

[31] G. L. Witt, R. Calawa, U. Mishara, and E. Weber, Eds., presented at the *Low Temperature (LT) GaAs and Related Materials Symp.*, 1992.

[32] B. Hillerich, "Shape analysis and coupling loss of microlenses on single-mode fiber tips," *Appl. Opt.*, vol. 27, no. 15, pp. 3102–3106, 1988.

T. Itoh (S-'69–M-'69–SM'74–F'82) received the Ph.D. degree in electrical engineering from the University of Illinois, Urbana, in 1969.

From September 1966 to April 1976, he was with the Electrical Engineering Department, University of Illinois. From April 1976 to August 1977, he was a Senior Research Engineer in the Radio Physics Laboratory, SRI International, Menlo Park, CA. From August 1977 to June 1978, he was an Associate Professor at the University of Kentucky, Lexington. In July 1978, he joined the faculty at the University of Texas at Austin, where he became a Professor of electrical engineering in 1981 and Director of the Electrical Engineering Research Laboratory in 1984. During the summer of 1979, he was a Guest Researcher at AEG-Telefunken, Ulm, West Germany. In September 1983, he was selected to hold the Hayden Head Centennial Professorship of Engineering at the University of Texas, and in September 1984, he was appointed Associate Chairman for Research and Planning of the Electrical and Computer Engineering Department. In January 1991, he joined the University of California at Los Angeles (UCLA), as Professor of electrical engineering and holder of the TRW Endowed Chair in Microwave and Millimeter Wave Electronics. He is currently Director of Joint Services Electronics Program (JSEP) and Director of Multidisciplinary University Research Initiative (MURI) program at UCLA. He was an Honorary Visiting Professor at Nanjin Institute of Technology, China, and at the Japan Defense Academy. In April 1994, he was appointed Adjunct Research Officer for Communications Research Laboratory, Ministry of Post and Telecommunication, Japan. He currently holds a Visiting Professorship at the University of Leeds, U.K., and is an External Examiner of the graduate program of the City University of Hong Kong. He has authored or co-authored over 220 journal publications, 380 refereed conference presentations, and has written over 20 books and book chapters in the area of microwaves, millimeter-waves, antennas and numerical electromagnetics.

L. Y. Lin received the M.S. and Ph.D. degrees in electrical engineering from the University of California at Los Angeles (UCLA), in 1993 and 1996, respectively.

In 1996, she joined the Lightwave Networks Research Department of AT&T Labs-Research, Red Bank, N.J., as a Technical Staff Member. She has published over 60 papers in technical journals and refereed conferences. Her research areas have include high-power high-speed photodetectors and micromachined free-space integrated optics. Her current research areas include switching for high-capacity optical transport networks and wavelength conversions.

Dr. Lin is a member of the Optical Society of America. She was the recipient of a GTE Fellowship from 1995 to 1996, and was awarded the Dr. Bor-Uei Chen's Memorial Scholarship from the Photonics Society of Chinese-Americans in 1995.

M. C. Wu received the M.S. and Ph.D. degrees in electrical engineering from the University of California at Berkeley, in 1985 and 1988, respectively.

From 1988 to 1992, he has been a Technical Staff Member at AT&T Bell Laboratories, Murray Hill, N.J., where he has conducted research in high-speed semiconductor optoelectronics. In 1993, he joined the faculty of the Electrical Engineering Department, University of California at Los Angeles (UCLA), as an Associate Professor. He has published over 80 papers in research journals, 110 papers in refereed conference proceedings, contributed one book chapter, and holds eight U.S. patents. His current research interests include micromachined optical systems, optical MEMS, ultrafast integrated optoelectronic devices, and microwave photonics.

Dr. Wu is a member of the American Physical Society, Optical Society of America, URSI, and Eta Kappa Nu. He has served as co-chair for the IEEE LEOS Summer Topical Meeting on Optical MEMS in 1996, and RF Optoelectronics in 1995. He has also served on the Program Committee of CLEO in 1996 and 1997, IEDM in 1996, and Photonic West in 1997. He was awarded the Packard Foundation Fellow in 1992, and the Meritorious Conference Paper Award of the 1994 GOMAC.

T. A. Vang received the B.S degrees in physics and electrical engineering from the University of Minnesota at Minneapolis, St. Paul, in 1985 and 1988, respectively, and the Ph.D. degree in electrical engineering from the University of Bradford, U.K., in 1993.

From 1988 to 1993, he was a Consultant to AT&T Bell Labs, Holmdel, NJ, working on GaAs-based OEICs. In 1994, he joined the Jet Propulsion Laboratory, Pasadena, CA, and is working on InP and GaAs OEICs and devices in the Photonics Technology Research Group.

R. E. Muller received the B.S. degree in chemical engineering from the University of Rochester, Rochester, NY, in 1984.

He has worked in photolithography process development at Commodore International and Microwave Semiconductor Corporation. In 1988, he joined the Jet Propulsion Laboratory, Center for Space Microelectronics, Pasadena, CA, where he is responsible for the operation of the JEOL JBX 5DII electron-beam lithography system, as well as related sample processing.

D. L. Sivco, photograph and biography not available at the time of publication.

A. Y. Cho received the B.S. M.S., and Ph.D. degrees in electrical engineering from the University of Illinois, Urbana.

In 1968, he joined Bell Laboratories, Murray Hill, N.J., as a Technical Staff Member, and was promoted to Department Head in 1984. He was named Director of the Materials Processing Research Laboratory in 1987, and in 1990 became Director of Semiconductor Research. His pioneering work on molecular beam epitaxy (MBE) has had a significant impact on the semiconductor industry, leading to the making of faster and more efficient electronic and optoelectronic semiconductor devices.

Dr. Cho has received many awards from technical and professional societies, including the 1982 International Prize for New Materials from the American Physical Society, the 1987 Solid-State Science and Technology Medal of the Electrochemical Society, the 1988 World Materials Congress Award, the 1990 International Crystal Growth Award of the American Association for Crystal Growth, the 1993 National Medal of Science, presented by President Clinton, the 1994 IEEE Medal of Honor, and the 1995 C&C (Computer and Communications) Prize, Japan.